Winding Function Theory Based Thrust Calculation on Nested-loop Secondary Linear Machine Adapted to Linear Metro

Yaping Zhang, Jian Ge, *Member, IEEE*, Wei Xu, *Senior Member, IEEE*, Hao Tang, Yang Gao, Xiaoliang Chen, Shihu Su, and Zhen Bao

***Abstract*—With advantages of strong drive capability, nested-loop secondary linear machine (NLS-LM) has great potentiality in linear metro. For its secondary structure with multiple loops, it is difficult to calculate the electromagnetic thrust of NLS-LM reasonably. Hence, in this paper, one thrust calculation method is proposed considering variable loop inductance and transient loop current. Firstly, to establish the secondary winding function, the modeling domain is confined to a limited range, and the equivalent loop span is employed by analyzing the coupling relationship between primary and secondary. Then, in order to obtain the secondary flux density, the transient secondary current is solved based on the loop impedance and induced voltage. Finally, the electromagnetic thrust can be calculated reasonably by the given primary current sheet and the calculated secondary flux density. Comprehensive simulations and experiments have demonstrated the effectiveness of the proposed method.**

***Index Terms*—Nested-loop secondary, Linear metro, Electro-magnetic thrust, Finite element algorithm (FEA), Transient nested-loop current, Winding function.**

NOMENCLATURE

Physics variables

A	Magnetic vector potential
B	Magnetic flux density
E	Induced voltage
f	Frequency
F_P	Primary magnetomotive force
I/i	Amplitude/instant value of phase current
j	Current sheet
k_{mutual}	Variation rate of the mutual inductance
k_{self}	Variation rate of the self-inductance
k_{wv}	Primary winding factor
k_Λ	End permeance factor
L	Longitudinal length of the primary iron core
L_{self}	Self-inductance of the nested-loop
M	Mutual inductance
M_{oim}	Peak value of the mutual inductance between the entry and exit loops
N_{ph}	Series turns per phase
p	Pole-pairs of primary windings
s_w	Slip
t_s	Time within one variation period of nested-loops distribution
T_e	Electromagnetic thrust
$T_{e,pul}$	Thrust generated by pulsating magnetic field
T_s	Variation period of nested-loop distribution
v	Pole-pair number of spatial harmonics
v_s	Secondary operating speed
w_s	Secondary slot pitch
x_{c0}	Initial position of the center-line of Nest 1
x_s	Entry-conductor position of secondary loop
y_c	Coil pitch in terms of slot number
$y_l / y_l^{'}$	Mechanical/Equivalent secondary loop span
Z	Total number of slots
δ_e	Electromagnetic air gap length
Δt	Sampling time interval
φ	Spatial phase
λ_{end}	Specific end-permeance
μ_0	Vacuum permeability

Subscripts

ab	The *b*th loop of the *a*th nest (excitation loop)
end	End-loop
jk	The *k*th loop of the *j*th nest (induction loop)
l	Nested-loop
m/*n*	Nest/loop number
M	Phase A, B or C
out	Nested-loop completely outside the air gap
p/*c*	Power/Control winding

Manuscript received February 22, 2023; revised April 18, 2023; accepted May 15, 2023. Date of publication June 25, 2023; Date of current version June 16, 2023.

This work was supported in part by the National Natural Science Foundation of China under Grants 52277050, and the Shenzhen International Collaboration under Grant GJHZ20210705142539007. (*Corresponding author: Jian Ge*)

Yaping Zhang, Jian Ge, Wei Xu, and Zhen Bao are with the State Key Laboratory of Advanced Electromagnetic Technology, School of Electrical and Electronic Engineering, Huazhong University of Science and Technology, Wuhan 430074, China (e-mails: yapingzhang@hust.edu.cn, gejian1994@hust.edu.cn, weixu@hust.edu.cn, d202180638@hust.edu.cn).

Hao Tang is with Xiangyang CRRC Motor Technology Co., Ltd., Xiangyang 441000, China, and also with CRRC Zhuzhou Institute Co., Ltd., Zhuzhou 412001, China (e-mail: tanghao@csrzic.com).

Yang Gao and Xiaoliang Chen are with Guangzhou Metro Group Co., Ltd, Guangzhou 510330, China (e-mail: gaoyang@gzmtr.com, chenxiaoliang@gzmtr.com).

Shihu Su is with the Zhuzhou CRRC Times Electric Co., Ltd. and CRRC Zhuzhou Motor Co., Ltd., Zhuzhou 412001, China (e-mail: sushihu@crrcgc.com)

Digital Object Identifier 10.30941/CESTEMS.2023.00042

P/s	Primary/ Secondary
w	Subscript *p* or *c*

I. Introduction

LINEAR metro, as developed very quickly during the past twenty years, has played an important role in alleviating urban traffic congestion and promoting economic and social development [1], [2]. As the key indicators of traction system, the carrying capacity and energy consumption of the vehicle are largely dependent on the linear machine. Among all types of linear machines, the linear machine with nested-loop secondary (NLS-LM) can theoretically make up for many defects of widely used linear induction machines (LIMs), for example, the electromagnetic thrust and efficiency of LIMs are significantly reduced at high speed with large slip [3]-[5], etc. The NLS-LM combines the operating characteristics of induction and synchronous machines, where the output power can be controlled by adjusting voltage and current of power winding (PW) and control winding (CW). And the secondary loop is a short-circuit structure without the requirement of external inverter. Those characteristics make NLS-LM drive system has the advantages of more adjustable power factor, stronger drive capability [6], etc. Thus, NLS-LM has great potentiality in linear metro.

Till now, just a few literatures have discussed the topics related to the thrust calculation of NLS-LM [4]-[8]. The NLS-LM is evolved from rotary machines (RM), by referring to the parameter analysis of RM, the basic principles for both design and stable operation of NLS-LM can be obtained [5]. To further explain the general rules of electromotive force and magnetomotive force (MMF) affected by the open primary core, the short primary winding theory is presented in [7], which provides a theoretical basis to calculate NLS-LM primary parameter. Then, in [8], the asymmetry of three-phase winding and the shifted slot vector affected by the end is analyzed to clarify the physical process of thrust ripple. However, the aforementioned researches ignore variable inductances and transient induced currents of nested-loops as entering and leaving the air gap. The analysis results of NLS-LM thrust are obtained by finite element algorithm (FEA) simulation or experiment. The variation of nested-loop secondary electromagnetic parameters affected by the end is lack of research, for this reason, it is difficult to estimate NLS-LM thrust reasonably.

To predict NLS-LM thrust, the estimation on electromagnetic parameters of nested-loop secondary is important but incomplete. The electromagnetic parameters under end effect have been studied on other types of linear motors, but the related methods have limitations for NLS-LM [9]-[17]. For instance, the magnetic flux generated by LIM secondary is analyzed by constructing an equivalent and unified current sheet based on wavelet and Fourier transform technique [9]-[12]. And the electromagnetic parameters of linear synchronous machine (LSM) are generally analyzed by subdomain model. However, the analysis method on LIM relies on its secondary property, the electroconductivity is constant and continuous along the motion direction [13], [14]. On the contrary, the operation principle and structure of the nested-loop secondary are quite different. Due to the independent loop structure, along the direction of movement, the resistivity of the nested-loop secondary sheet is not a constant. Considering magnetic regarded as a stable MMF source as the LSMs due to dynamic secondary currents generated by the electromagnetic induction [16]. Hence, the secondary electromagnetic analysis methods of LIMs are not applicable for the NLS-LM, the subdomain model approach is also incompatible with NLS-LM [17].

The aforementioned methods cannot describe the complex variation of nested-loop secondary parameters, such as secondary inductance and induced voltage. And the transient secondary current in the process of nested-loop passing through the air gap is not considered by the existing researches. Moreover, the effective calculation on variable secondary parameters is very important for the NLS-LM thrust computation. Motivated by this, a thrust calculation method for NLS-LM combined with transient secondary current analysis is proposed in this paper, and main innovations are summarized as follows:

1) It is proved that for NLS-LM, the primary windings are mainly coupled with the air gap magnetic field, which can reduce the number of objective nests and nested-loop secondary inductance matrix orders, and simplify the complexity of the thrust calculation method as much as possible.

2) Based on the proof of the primary-secondary coupling relationship, the equivalent end-loop span is defined for the improved secondary winding function. Then an improved winding function of nested-loop secondary is derived for NLS-LM to further analyze the variation of secondary electromagnetic parameters effectively.

3) In order to realize the magnetic flux density calculation on nested-loop secondary, the nested-loop current calculation method is presented by recursive method. Subsequently, NLS-LM thrust is established with the given primary current sheet and the estimated secondary current. The proposed comprehensive calculation method on secondary parameters is very important for the design and optimization of NLS-LM.

The remainder of this paper is organized as follows: Section II analyzes the magnetic coupling relationship between primary windings and nested-loops, and constructs the nested-loop secondary winding functions with some proper assumptions. Based on the winding theory, the calculation methods of nested-loop secondary parameters and NLS-LM thrust are fully investigated in Section III. In order to verify the reliability of the proposed thrust calculation method, FEA simulation and experiments are carried out in Section IV. Finally, brief conclusions are drawn in Section V.

II. Modeling of Secondary Winding Function

A. Operation Principle of the NLS-LM

In the NLS-LM, the nested loops can modulate the air gap magnetic field to generate electromagnetic thrust and convert energy. Similar to the stable operation condition of RM, the secondary moving speed of NLS-LM satisfies

$$v_s = \frac{f_p \pm f_c}{p_p \pm p_c} L \tag{1}$$

When the machine operates at steady state. Therein, f_p and f_c can be positive or negative, which represents different phase sequences of primary windings. Typically, some nested loops of secondary are completely located outside of the air gap due to the finite length of the primary iron core, which is different with the corresponding RM. Therefore, it is necessary to analyze whether such nested loops have a large impact on the electromagnetic thrust at first.

B. Discussion on Outside Nested-loops

In order to simplify the calculation process and highlight the main problems, some assumptions are made as follows:

1) The influence of slot-opening is corrected by the Carter's coefficient.
2) The permeability of iron core μ_{Fe} is infinite, and the core loss ignored.
3) The value of nested-loop resistance is constant.
4) The carrying current is located at a certain point on the midline of air gap with the section area of conductor neglected.
5) The flux density is distributed evenly within the transverse width D.
6) The secondary moving speed is constant.

The MMFs F_P generated by the primary winding of NLS-LM comprise traveling and pulsating components [7], as expressed by

$$F_{P,M,w} = 2N_{ph,w}i_{M,w}\left[\frac{k_{wv,w}}{v\pi}\cos\left(\frac{2\pi v}{L}x+\varphi_{M,w}\right) + \frac{k_\Lambda y_{c,w}}{Z(2k_\Lambda+L)}\right] \tag{2}$$

According to the direction of movement, the entry end is set as the origin of the coordinate system in this paper. For the region out of air gap, the specific end-permeance λ_{end} can be approximately obtained as [18]

$$\lambda_{end} \approx \begin{cases} \sqrt{1+\left(\frac{\pi x}{4\delta_e}\right)^2}+\frac{\pi x}{4\delta_e} & x \le 0 \\ \sqrt{1+\left[\frac{\pi(x-L)}{4\delta_e}\right]^2}-\frac{\pi(x-L)}{4\delta_e} & x \ge L \end{cases} \tag{3}$$

Combined with eqs. (2) and (3), the mutual inductance between primary winding and outside nested loop can be derived as

$$M_{sP,M,w} = \int_{x_s-\frac{y_l}{2}}^{x_s+\frac{y_l}{2}} \frac{\mu_0 F_{P,M,w}\lambda_{rel}}{\delta_e i_{M,w}}\mathrm{d}x \tag{4}$$

As shown in Fig. 1, the specific end-permeance λ_{end} reduces sharply when the position is away from the primary iron core, making the mutual inductance between primary winding and outside nested loop approach zero. It can be inferred reasonably that the outside nested loop, hardly coupled with the primary windings, contributes little electromagnetic thrust, which can be thereby neglected during the calculation. Consequently, only nested loops as fully or partially located in the air gap are considered into this study, as illustrated as follows.

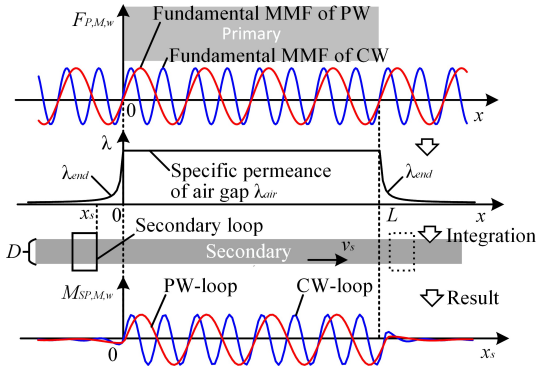

Fig. 1. Coulpling relationship between primary winding and secondary loop.

C. Winding Function of Nested-loop Secondary

Based on the aforementioned analysis, the boundaries of the nested-loop secondary are set at the entry nest and exit nest, respectively. In this way, the domain of the secondary winding function is confined to a limited range, which effectively reduces the dimensionality of the secondary inductance matrix. In this paper, the pole-pair numbers p_p and p_c are designed as 2 and 4, respectively. And each nest consists of three loops, as shown in Fig. 2. The nests are numbered sequentially along the direction of movement, and the loops are numbered in order of spans, from smallest to largest.

The distribution of nested-loop secondary in the air gap is dynamically changing due to the finite primary length. And the variation period T_s of nested-loops distribution depends on the nest pitch τ_s and motion velocity v_s, as defined by

$$T_s = \frac{\tau_s}{v_s} \tag{5}$$

For any operating time t, the nested-loop distribution can be judged by t_s, as given by

$$t_s = \mathrm{Mod}\left(\frac{t}{T_s}\right) = \mathrm{Mod}\left(\frac{v_s t}{\tau_s}\right), t_s \in [0, T_s] \tag{6}$$

where Mod represents modulo operation. By the derivation method of (2), the MMF generated by a current-carrying conductor of nested-loop secondary can be derived as

$$\begin{aligned} &F_{mn}(x,t) = k_{0mn}i_{mn} + \sum_{v=1}^{\infty} k_{vmn}i_{mn}\cos\left(\frac{2v\pi}{L}x+\theta_{cmn}\right) \\ &\Rightarrow k_{0mn} = \frac{k_\Lambda(L-2x_{s,mn})}{L^2(k_\Lambda+1)}, k_{vmn} = \frac{2}{v\pi}\sin\frac{v\pi x_{s,mn}}{L} \\ &\Rightarrow \theta_{cmn} = -\frac{\pi v x_{s,mn}}{L}+\pi \end{aligned} \tag{7}$$

Besides, the entry conductor position of the nth loop of the mth nest can be calculated by

$$x_{s,mn} = x_{c0} + (m-1)\tau_s + \frac{y_{l,n}}{2} + v_s t_s \tag{8}$$

According to the relative position of the nested loop and the primary, the equivalent loop span $y'_{l,n}$, is defined as

$$y'_{l,n} = \begin{cases} 0 & ,x_{s,mn} \le 0, x_{s,mn} > L + y_{l,n} \\ v_s t_s & ,0 < x_{s,mn} \le y_{l,n} \\ y_{l,n} & ,y_{l,n} < x_{s,mn} \le L \\ y_{l,n} - v_s t_s & ,L < x_{s,mn} \le L + y_{l,n} \end{cases} \tag{9}$$

Combined with (7)-(9), the winding function of secondary

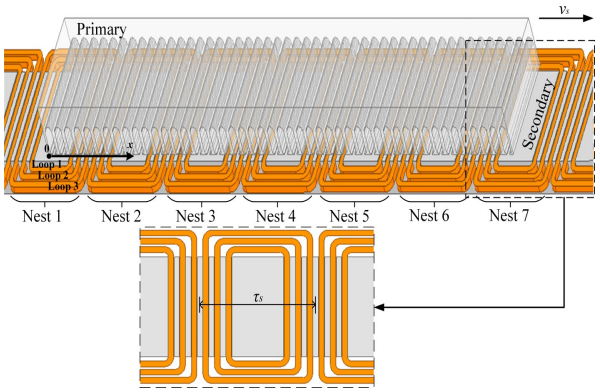

Fig. 2. Diagram of the nested-loop secondary.

loop can be obtained by

$$\begin{aligned} N_{mn}(x,t) &= \frac{F_{mn}\left(x_{s,mn}\right)-F_{mn}\left(x_{s,mn}-y_{l,n}^{'}\right)}{I} \\ &= \sum_{v=1}^{\infty} k_{s,n}\cos\left[\frac{2\pi v}{L}(x-v_s t_s)+\varphi_{s,m}\right]+N_{av,n} \\ \Rightarrow k_{s,n} &= \frac{-2}{v\pi}\sin\left(\frac{\pi v y_{l,n}^{'}}{L}\right), N_{av,n}=-\frac{2y_{l,n}^{'}k_{\Lambda}}{(1+k_{\Lambda})L^2} \\ \Rightarrow \varphi_{s,m} &= -\frac{2v\pi}{L}\left[x_{c0}+(m-1)\tau_s\right] \end{aligned} \tag{10}$$

It is mentioned that the nested-loop secondary winding function consists of two components, i.e., the first term is the spatial harmonic component and the second term the pulsating component. When the primary length L is fixed, pulsating component and the amplitude of spatial harmonic component are determined by the loop span $y_{l,n}$, while the phase of the spatial harmonic component is related to m, as determined by the nest position.

III. Thrust Calculation Based on Secondary Winding Function

The NLS-LM thrust can be obtained through the calculation process as illustrated in Fig. 3. Firstly, both the flux density and equivalent current sheet of primary are calculated according to the primary MMFs. Meanwhile, the secondary inductance is derived based on the secondary winding function as given in Section II. Secondly, the induced voltage of nested loops is obtained by integration of the primary flux density and the current is solved with the impedance matrix. Then, the secondary flux density is calculated by multiplication of secondary current and secondary winding function. Thirdly, the electromagnetic thrust is obtained by integration of primary current sheet and secondary flux density. In the above process, the key point is the calculation of the secondary inductance.

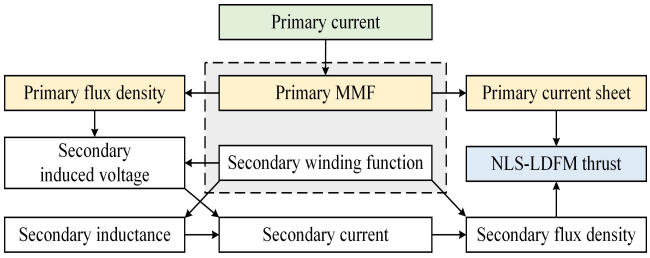

Fig. 3. The simple flow chart of the proposed method for the NLS-LM.

A. Secondary Self-inductance

When the nested-loops pass through the air gap, their inductances are not constant. For the nested-loop completely located in the air gap, its self-inductance can be derived by

$$\begin{aligned} L_{self,mn} &= \sum_{v=1}^{\infty}\frac{\mu_0 D}{\delta_e}\int_{x_{s,mn}-y_{l,n}}^{x_{s,mn}} N_{mn}(x,t)\,\mathrm{d}x \\ &= \sum_{v=1}^{\infty}\frac{\mu_0 D}{2\pi v\delta_e}\left[k_{s,n}L\left(\sin\varphi_1-\sin\varphi_2\right)-\frac{4\pi v y_{l,n}^2 k_{\Lambda}}{(1+k_{\Lambda})L^2}\right] \\ \Rightarrow \varphi_1 &= \varphi_{s,m}+\frac{2\pi v x_{s,mn}}{L} \\ \Rightarrow \varphi_2 &= \varphi_{s,m}+\frac{2\pi v\left(x_{s,mn}-y_{l,n}^2\right)}{L} \end{aligned} \tag{11}$$

For the nested-loops completely out of the air gap, the generated magnetic vector potential can be obtained by the method of images [19], as expressed by

$$A_{out,n}(x) = \frac{\mu_0 I_{out}}{2\pi}\ln\left(\frac{4\left(x-y_{l,n}\right)^2+\delta_e^2}{4x^2+\delta_e^2}\right) \tag{12}$$

Consequently, its self-inductance can be derived by

$$\begin{aligned} L_{out,n} &= D\int_{-y_{l,n}}^{0}-\frac{\partial}{\partial x}\frac{A_{out,n}}{I_{out}}\mathrm{d}x \\ &= \frac{\mu_0 D}{\pi}\ln\left(\frac{\delta_e^2}{4y_{l,n}^2+\delta_e^2}\right) \end{aligned} \tag{13}$$

It can be approximated that the self-inductance of the nested-loop changes linearly in the process of entering and leaving the air gap, which is related to $y_{l,n}$ and v_s. And the variation rate $k_{sel\text{-}f,mn}$ of the self-inductance in different loops is calculated by

$$k_{Self,mn} = \frac{\left(L_{self,mn}-L_{out,n}\right)v_s}{y_{l,n}} \tag{14}$$

B. Secondary Mutual Inductance

Based on the secondary winding function, the mutual inductance between the two loops completely located in the air gap can be given by

$$\begin{aligned} M_{ab,jk} &= \sum_{v=1}^{\infty}\frac{\mu_0 D}{\delta_e}\int_{x_{jk}-y_{l,b}}^{x_{ab}} N_{jk}(x,t)\,\mathrm{d}x \\ &= \sum_{v=1}^{\infty}\frac{\mu_0 D}{2\pi v\delta_e}\left\{2\pi v N_{av,k}y_{l,k}+k_{s,k}L\left[\sin\left(\varphi_{s,j}+\frac{2\pi v x_{ab}}{L}\right)\right.\right. \\ &\quad \left.\left.-\sin\left(\varphi_{s,j}+\frac{2\pi v\left(x_{ab}-y_{l,b}\right)}{L}\right)\right]\right\} \end{aligned} \tag{15}$$

In the subsequent analysis, the excitation loop and induction loop are denoted as *jk* and *ab*, respectively.

Due to the motion of secondary, Loop *ab* and Loop *jk* will not always locate in the air gap at the same time. Based on the equivalent loop span function (9), the mutual inductance can be approximated to 0 when the Loop *ab* or Loop *jk* is completely outside the air gap. When one of loops passing through the end, the mutual inductance can be considered varying linearly with the loop position. The variation rate can be calculated by

$$k_{mutual}=\frac{M_{ab,jk}v_s}{y_{l,end}+w_s} \tag{16}$$

However, the mutual inductance cannot be derived from (15) and (16) when both loops are partially located in the air gap. The mutual inductance could reach the peak value M_{oim} when both loops have half span inside the air gap, as calculated by

$$\begin{aligned}M_{oim}&=\sum_{v=1}^{\infty}\frac{\mu_0 D}{\delta_e}\int_0^{\frac{y_{l,b}}{2}}N_{jk}\left(x,t\right)\mathrm{d}x\\&=\sum_{v=1}^{\infty}\frac{\mu_0 D}{2\delta_e}\left\{N_{av,k}y_{l,b}+\frac{k_{s,k}L}{\pi v}\left[-\sin\left(\varphi_{s,j}\right)\right.\right.\\&\left.\left.+\sin\left(\varphi_{s,j}+\frac{\pi v y_{l,b}}{L}\right)\right]\right\}\end{aligned} \tag{17}$$

Similarly, the mutual inductance between the entry and exit loops can be derived by

$$M_{fl}=\begin{cases}\dfrac{2M_{oim}}{T_s}t_s & 0\le t_s<\dfrac{T_s}{2}\\ M_{oim}-\dfrac{2M_{oim}}{T_s}\left(t_s-\dfrac{T_s}{2}\right) & \dfrac{T_s}{2}<t_s\le T_s\end{cases} \tag{18}$$

C. Secondary Current

According to the above discussion, the induced voltage E_s of the nth loop in the mth nest can be derived by

$$E_s\left(t\right)=\sum_{w}^{p,c}\sum_{M}^{A,B,C}\frac{\partial}{\partial t}\int_{x_{mn0}-y_{l,n}^{'}+v_s t}^{x_{mn0}+v_s t}\sum_{v=1}^{\infty}\frac{\mu_0 F_{P,M,w}}{\delta_e}\mathrm{d}x \tag{19}$$

Due to the segmental feature of the equivalent loop span $y_{l,n}^{'}$, the derivation results for the loops located at end side or entirely in the air gap are different, as shown in (A.1), (A.2), and (A.3), respectively. Besides, the nested-loop induced voltage functions have the following characteristics:

1) For the entry and exit end loops, the pulsating components are calculated in the same way.

2) For all loops, the amplitudes of spatial harmonic component are calculated in the same way.

3) For all the loops, the main difference is reflected in the phases of the spatial harmonics.

Furthermore, the nested-loop induced current is always working in a dynamic state. When the motion velocity v_s is small, the induced current of entry loop increases from zero to the steady state. When the loop leaves the air gap, the current will decay to zero. However, when the value of motion velocity v_s is large, the induced current may not reach the steady state, and the transient current is always related to its value at the previous moment. For this issue, the nested-loop induced current calculation method is given by recursive conception, as shown in Fig. 4. When the operating speed is constant, the distribution of the nested-loops in the air gap is periodic. At the beginning of distribution period, the loop position needs to be reset to its initial value, and the loop current is updated. As seen from this figure, it mainly contains three steps as follows:

1) The initial values of the nested-loop induced voltage and current are set to zero, and time discretization is performed using sampling time interval Δt.

2) The initial current value for new distribution period needs to be reset, when the analyzed nested-loop distribution is in a new period judged by (A.4). The initial current of the loop in the mth nest is updated as that of the loop with the same span in (m-1)th nest. Then, the initial currents of enter loops are reset as zero. In this way, every loop current value for every nested-loop distribution period updates dynamically.

3) The induced current is derived by the recurrence equation (A.5). If the desired time $t_{analysis}$ is not calculated, it will return to step 2 at the next sampling time.

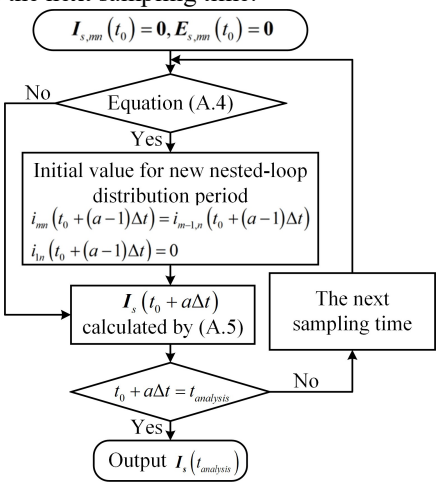

Fig. 4. Flowchart of secondary current calculation for NLS-LM.

D. Electromagnetic Thrust Calculation

According to the previous analysis, the NLS-LM thrust can be calculated by integrating the primary current sheet with the secondary flux density. Combined with (2), the primary current sheet can be calculated by

$$\begin{aligned}j_{P,M,w}\left(x,t\right)&=\frac{\partial F_{P,M,w}}{\partial x}\\&=-\sum_{v=1}^{\infty}\frac{4i_{M,w}k_{wv,w}N_{ph,w}\sin\left(\dfrac{2\pi v}{L}x+\varphi_{M,w}\right)}{L}\end{aligned} \tag{20}$$

According to the superposition principle, the secondary air gap flux density can be obtained by summing the flux density generated by all loops, as defined by

$$B_s\left(x,t\right)=\frac{\mu_0}{\delta_e}\sum_{mn}^{m_{\max}n_{\max}}N_{mn}\left(x,t\right)i_{mn}\left(t\right) \tag{21}$$

Further, the electromagnetic thrust T_e can be derived as

$$\begin{aligned}&T_e=\sum_{w=p,c}\sum_{M=A,B,C}\sum_{mn}^{m_{\max}n_{\max}}T_{swM,mn}\\&\Rightarrow T_{swM,mn}=D\int_0^{L}j_{P,M,w}\left(x,t\right)B_s\left(x,t\right)\mathrm{d}x\\&\quad=-\sum_{v=1}^{\infty}T_{mag}\sin\left(\varphi_{M,w}-\varphi_{s,m}+\frac{2\pi v}{L}v_s t_s\right)\\&\Rightarrow T_{mag}=\frac{2\mu_0}{\delta_e}Di_{M,w}i_{mn}k_{wv,w}N_{ph,w}k_{s,n}\end{aligned} \tag{22}$$

where $T_{swM,mn}$ is the thrust generated by the nth loop in the mth nest. Moreover, the thrust generated by pulsating magnetic field can be derived by

$$T_{e,pul} = -D\sum_{w=p,c}^{m_{\max}n_{\max}}\sum_{mn}\int_0^L j_{P,M,w}(x,t)B_{s,av}(x,t)\,\mathrm{d}x$$
$$= D\sum_{w=p,c}^{m_{\max}n_{\max}}\sum_{mn}\int_0^L j_{P,M,w}(x,t)\frac{\mu_0}{\delta_e}\frac{2y'_{l,n}k_\Lambda}{(1+k_\Lambda)L^2}i_{mn}\,\mathrm{d}x = 0 \quad (23)$$

As shown in (23), the pulsating magnetic field does not generate average thrust.

IV. Simulation and Experiments

In this section, the validity of the thrust calculation results is fully demonstrated by comparing with related FEA simulation and experimental results under different typical working states. The structural parameters of FEA simulation are the same with NLS-LM prototype, as given in Table I. In order to reduce the space and construction cost, the primary is designed as arc-shape structure with 1.154 meter diameter, as shown in Figs. 5 and 6, respectively, where the circular movement of nested-loop secondary can be approximated as linear movement. Combined with (1), the span of one nest containing three loops is designed to be one-sixth of the primary longitudinal length, since the nest number is the sum of primary winding pole-pairs without cut-open primary. For the platform, Primary1 is powered via back-to-back converter, and the windings of Primary2 are open-circuited. Besides, the permanent magnet synchronous machine (PMSM) is selected as the load machine for the NLS-LM, which can operate as a generator with braking torque to NLS-LM without extra power supply. The shafts of NLS-LM and PMSM are connected through the velocity and thrust sensor. Meanwhile, the PMSM is connected to load resistance through voltage regulator. And the load resistance of PMSM is changed by the voltage regulator which can adjust the working load equivalently.

Table I
Main Specifications of the NLS-LDFM

Name	Value
Number of slots	48
Number of PW poles	2
Number of CW poles	4
Single coil turns of PW	16
Single coil turns of PW	31
Height of primary core (mm)	57
Longitudinal length of primary core (mm)	900
Height of primary core (mm)	57
Transversal length of LDFM (mm)	125
Air gap length (mm)	8
Conductivity of the secondary loop (S/m)	1.7 × 10−8

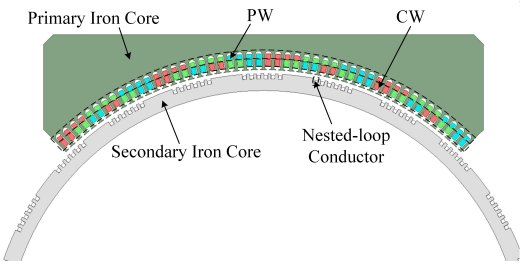

Fig. 5. FEA simulation for the NLS-LM.

By changing the power supply, the NLS-LM can operate in asynchronous or synchronous mode. For the asynchronous mode, the PW or CW is set open-circuited or symmetric short-circuited, and the slip can be calculated by

$$s_w = \frac{(f_w/p_w)L - v_s}{(f_w/p_w)L} \quad (24)$$

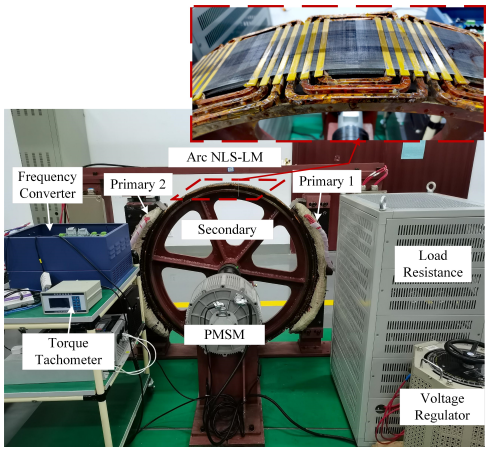

Fig. 6. Arc NLS-LM platform.

For the synchronous mode, the PW is powered by ac source, and the CW is powered by ac or dc source. The excitation parameters for experiment are listed in Table II. Besides, all the proposed thrust calculation and FEA simulation are based on experimental winding current data. For the short-circuited or voltage powered windings, the fast Fourier transformation (FFT) is performed on their current waves to obtain the phase angle and amplitude.

The thrust under asynchronous mode is shown in Figs. 7 and 8, respectively. It can be seen that the thrust based on the winding function theory (WF) is consistent with that from FEA. Comparing with the experimental results, the maximum relative errors of thrust calculations for the two asynchronous

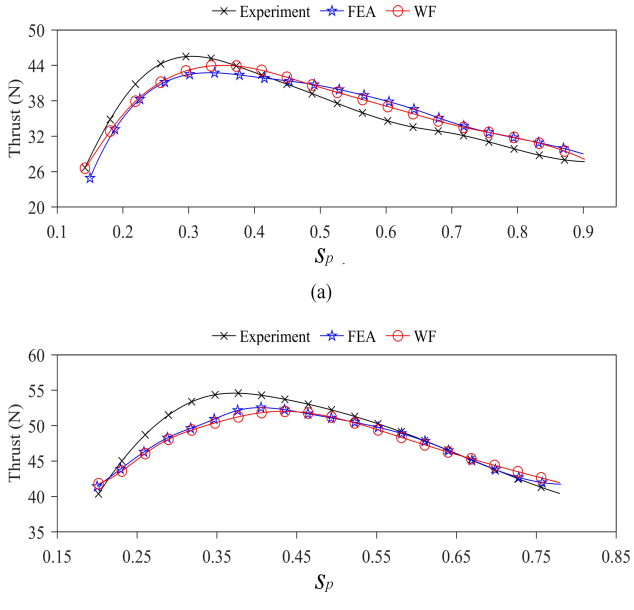

Fig. 7. Thrust for asynchronous mode with open-circuited CW. (a) 25Hz excited PW. (b) 15Hz excited PW.

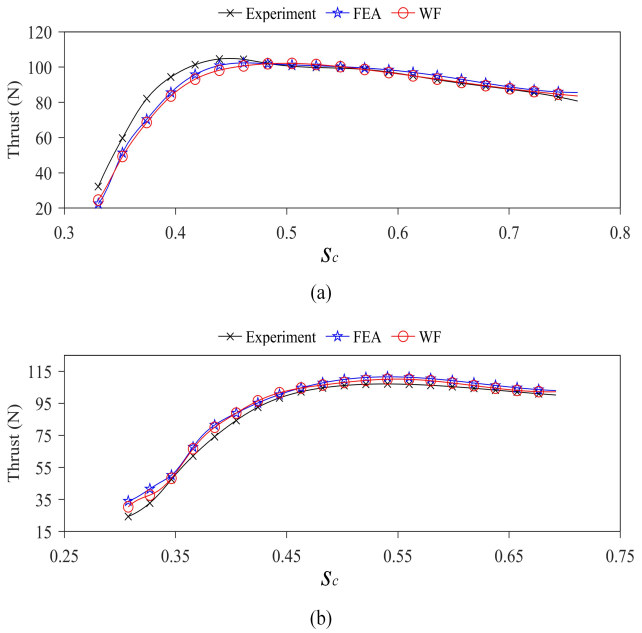

Fig. 8. Thrust for asynchronous mode with short-circuited PW. (a) 50Hz excited CW. (b) 40Hz excited CW.

TABLE II
EXCITATION PARAMETERS OF EXPERIMENT

Operation mode	PW amplitude / frequency	CW amplitude / frequency
Asynchronous	21.21A / 25Hz & 15Hz	Open-circuit
Asynchronous	Short-circuit	23.5A / 50Hz & 40Hz
Synchronous	22A; 50Hz	11.31A / 0Hz
Synchronous	28 ~ 71V/ – 20 ~ 15Hz (V/f ≈ 3)	169.71V / 50Hz

modes are 14.11% and 25.08%, respectively. For the asynchronous mode with short-circuited PW, the measured short-circuit current needs FFT to obtain the amplitudes and phases of the main harmonics. It indicates that the selected number of FFT components can also lead to a little deviation between the calculation and experiment thrust, since the calculated winding current is smaller than its actual value. And assembly problems could bring some difference between calculation and experimental thrust. For example, the air gap length of prototype is about 6.1~ 8.5mm, and the actual average length is less than the design value, which could generate larger electromagnetic thrust in practice. Meanwhile, the transversal length is about 115 120mm due to axial assembly deviation. It could decrease the electromagnetic thrust to some extent. Furthermore, the deformation of the secondary shaft can also result in significant errors between the calculated and experimental thrust. This deformation leads to air gap variations, which generate additional harmonics of magnetic flux density and ultimately impact the induced currents of primary windings and nested-loops. To reduce such errors, precise primary current and machine topology parameters are required. However, it is challenging to measure the uneven air gap caused by shaft deformation, and also difficult to correct the nested-loop current harmonics resulting from it. Therefore, large relative errors still persist between the experimental results and theoretical calculations and simulations. Despite the relative errors between the calculated and experimental thrust, the simulation results presented in this paper are in high agreement with the calculated results, demonstrating the effectiveness of the proposed method and suggesting a more accurate means of calculating the electromagnetic thrust of NLS-LMs.

In addition, the calculation of the secondary inductance is very important for thrust calculation of the NLS-LM. Since the secondary inductance cannot be measured by the experimental platform, the results from calculation procedure are compared with that from FEA simulation. The self-inductance results for the loops with different span are given in Fig. 9. And the results of mutual inductances are given in Fig. 10. The left dashed line stands for the entry boundary, and the right dashed line represents the exit boundary. As seen from Fig. 10(a), Curve 1 represents the mutual inductances between Loop 1 in Nest 1 and Loop 1 in Nest 7. Meanwhile, Curve 2 stands for mutual inductances between Loop 1 in Nest 2 and Loop 1 in Nest 4. And x_{rc0} is the initial position of the right conductor of the Loop 1 in Nest 2. It can be seen that the trends of the self-inductance curves obtained by FEA simulation and the proposed calculation method are approximately the same. Since the iron core permeability is assumed as infinite, the calculated inductances for the loops as fully located in the air gap are larger than those from simulation. And the inductance variation rate is approximately regarded as a constant, which is the main cause of the deviation for the calculated inductance at the air gap

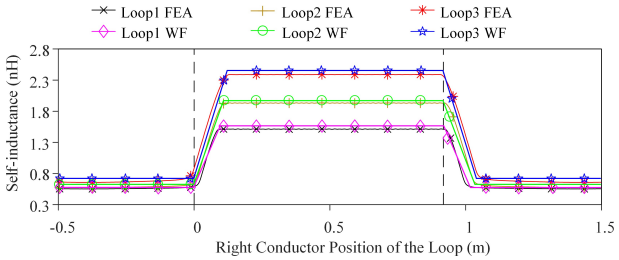

Fig. 9. The self-inductance for one nest.

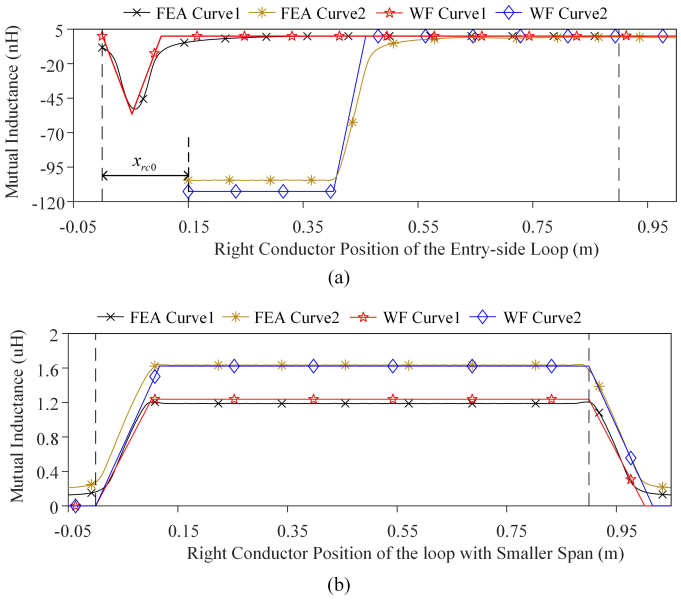

Fig. 10. Mutual inductance for nested-loops. (a) The loops in different nests. (b) The loops in the same nest.

boundary. Furthermore, the deviation process of the calculated inductance could reduce the secondary currents, and bring some error to current phase, which would finally reduce the thrust in theory.

Fig. 11 and Table III show the thrust under two synchronous modes. For the first synchronous mode, the primary current parameters can be directly applied to the calculation program without FFT processing, since the PW and CW are powered by the current sources. And the maximum relative errors for the two synchronous modes are 10.51% and 15.82%, respectively. Meanwhile, it is difficult to obtain the secondary initial position at the time of velocity stabilization during the experiment, which would bring some deviations to the calculated thrust. Additionally, proposed method for thrust calculation of NLS-LM in the paper exhibits a high level of agreement with the finite element simulation results. Both the proposed method and finite element simulation are transient calculations in discrete time, which require setting a stop time and time step. However, the proposed method provides explicit analytical formulas for the electromagnetic parameters of NLS-LM, while the finite element simulation requires meshing and numerical computation for each grid, and the accuracy of the meshing greatly affects the simulation results. In this case, the proposed method can greatly save computer storage and computational resources, and the computation time for each discrete time step is shorter, resulting in higher computational efficiency compared with the finite element method.

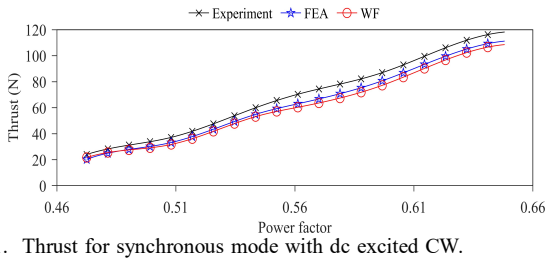

Fig. 11. Thrust for synchronous mode with dc excited CW.

TABLE III
THRUST FOR SYNCHRONOUS MODE WITH TWO *AC* EXCITED WINDINGS

U_p (V)	f_p (Hz)	v_s (m/s)	Thrust (N)		
			Calculation	Experiment	Simulation
42.43	10	8.94	100.42	114.94	108.79
56.57	15	9.68	53.15	63.14	54.27
28.28	-5	6.70	187.63	196.00	178.46
42.43	-10	5.96	235.11	242.98	238.84
56.57	-15	5.21	257.57	265.72	258.39
70.71	-20	4.47	271.84	278.57	269.02

V. CONCLUSIONS

In this paper, one electromagnetic thrust calculation method for NLS-LM is presented in terms of nested-loop secondary winding function. By introducing the equivalent loop span, the secondary winding function is established by the winding function theory, and then the corresponding calculation procedure of secondary flux density is put forward. Furthermore, the electromagnetic thrust can be obtained, comprehensively taking the variation of loop inductance and the transient loop current into consideration. Also, the theoretical calculation results are mostly consistent with simulation and experiment results, which indicates that the proposed electromagnetic thrust calculation method is generally reasonable, and can effectively obtain the electromagnetic thrust under different operation modes. Comprehensive simulation and experiments have fully demonstrated that the proposed method for electro- magnetic thrust estimation can get much higher accuracy under current excitation than that under voltage excitation, which can be used as an alternative to FEA for NLS-LM.

APPENDIX

The induced voltage $E_{s,in}$ of the nth loop in the mth nest located entirely in the air gap is expressed by

$$\begin{aligned}
E_{s,in}(t)= E_{sav,p} &- \sum_{v=1}^{\infty} E_{sM1,p}\left[\cos\left(\omega_2 t+\varphi_{2,p}\right)-\cos\left(\omega_2 t+\varphi_{2,n,p}\right)\right] \\
&- \sum_{v=1}^{\infty} E_{sM2,p}\left[\sin\left(\omega_2 t+\varphi_{2,p}\right)-\sin\left(\omega_2 t+\varphi_{2,n,p}\right)\right]+E_{sav,c} \\
&- \sum_{v=1}^{\infty} E_{sM1,c}\left[\cos\left(\omega_2 t+\varphi_{2,c}\right)-\cos\left(\omega_2 t+\varphi_{2,n,c}\right)\right] \\
&- \sum_{v=1}^{\infty} E_{sM2,c}\left[\sin\left(\omega_2 t+\varphi_{2,c}\right)-\sin\left(\omega_2 t+\varphi_{2,n,c}\right)\right] \\
\Rightarrow E_{sav,w} &= \sum_{M}^{A,B,C} \frac{2\sqrt{2}\pi\mu_0}{\delta_e} D y_{l,n} f_w \frac{k_\Lambda y_{c,w}}{Z(2k_\Lambda+L)} I_{P,w,M} e^{j\varphi_{i,w,M}} \\
\Rightarrow E_{sM1,w} &= \sum_{M}^{A,B,C} \frac{2\sqrt{2}\mu_0}{v\pi\delta_e} D I_{P,w,M} N_{ph,w} k_{wv,w} v_s \cos\left(2\pi f_w t+\varphi_{i,w,M}\right) \\
\Rightarrow E_{sM2,w} &= \sum_{M}^{A,B,C} \frac{\sqrt{2}\mu_0 D}{v^2\pi^2\delta_e} L N_{ph,w} k_{wv,w} I_{P,w,M} \sin\left(2\pi f_w t+\varphi_{i,w,M}\right) \\
\Rightarrow \omega_2 &= \frac{2\pi v}{L} v_s, \varphi_{2,w}=\varphi_{Mv,w}+\frac{2\pi v x_{mn}}{L}, \varphi_{2,n,w}=\varphi_{Mv,w}+\frac{2\pi v\left(x_{mn}-y_{l,n}\right)}{L}
\end{aligned} \tag{A.1}$$

where f_w is the frequency of primary current, I_P and φ_i are the root mean-square (RMS) values and phase angles of winding current, respectively. The induced voltage of the entry loop is deduced as

$$\begin{aligned}
E_{s,en}(t)=E_{eav,p} &- \sum_{v=1}^{\infty} E_{sM1,p}\left[\cos\left(\omega_2 t+\varphi_{2,p}\right)-\cos\left(\omega_2 t+\varphi_{en,n,p}\right)\right] \\
&- \sum_{v=1}^{\infty} E_{sM2,p}\left[\sin\left(\omega_2 t+\varphi_{2,p}\right)-\sin\left(\omega_2 t+\varphi_{en,n,p}\right)\right]+E_{eav,c} \\
&- \sum_{v=1}^{\infty} E_{sM1,c}\left[\cos\left(\omega_2 t+\varphi_{2,c}\right)-\cos\left(\omega_2 t+\varphi_{en,n,c}\right)\right] \\
&- \sum_{v=1}^{\infty} E_{sM2,c}\left[\sin\left(\omega_2 t+\varphi_{2,c}\right)-\sin\left(\omega_2 t+\varphi_{en,n,c}\right)\right] \\
\Rightarrow E_{eav,w} &= \sum_{M}^{A,B,C} \frac{2\sqrt{2}\pi\mu_0}{\delta_e} D y'_{l,n} f_w \frac{k_\Lambda y_{c,w}}{Z(2k_\Lambda+L)} I_{P,w,M} e^{j\varphi_{i,w,M}-\frac{\pi}{2}} \\
\Rightarrow \varphi_{en,n,w} &= \varphi_{Mv,w}+\frac{2\pi v\left(x_{mn0}-y'_{l,n}\right)}{L}
\end{aligned} \tag{A.2}$$

The induced voltage of the exit loop can be described by

$$
\begin{aligned}
E_{s,ex}(t) &= E_{eav,p} - \sum_{v=1}^{\infty} E_{sM1,p}\left[\cos\left(\omega_2 t+\varphi_{ex,p}\right)-\cos\left(\omega_2 t+\varphi_{2,n,p}\right)\right] \\
&\quad - \sum_{v=1}^{\infty} E_{sM2,p}\left[\sin\left(\omega_2 t+\varphi_{ex,p}\right)-\sin\left(\omega_2 t+\varphi_{2,n,p}\right)\right] + E_{eav,c} \\
&\quad - \sum_{v=1}^{\infty} E_{sM1,c}\left[\cos\left(\omega_2 t+\varphi_{ex,c}\right)-\cos\left(\omega_2 t+\varphi_{2,n,c}\right)\right] \\
&\quad - \sum_{v=1}^{\infty} E_{sM2,c}\left[\sin\left(\omega_2 t+\varphi_{ex,c}\right)-\sin\left(\omega_2 t+\varphi_{2,n,c}\right)\right] \\
\Rightarrow \varphi_{ex,w} &= \varphi_{Mv,w} + \frac{2\pi v\left(x_{mn0}-y'_{l,n}\right)}{L}
\end{aligned}
\tag{A.3}
$$

As for the analysis of secondary current, whether the nested-loop distribution at the *i*th sampling time is in the new period is judged by

$$
\mathrm{Fix}\left(\frac{t_0+i\Delta t}{T_s}\right)-\mathrm{Fix}\left(\frac{t_0+(i-1)\Delta t}{T_s}\right)=1 \tag{A.4}
$$

where Fix stands for floor function towards zero.

The recurrence function for the induced current of nested-loop secondary is described by

$$
\begin{aligned}
\boldsymbol{I}_s(t_0+i\Delta t) &= \begin{bmatrix} i_{11} & i_{12} & \cdots & i_{m_{\max}n_{\max}} \end{bmatrix}^T \\
&= \frac{\boldsymbol{E}_{s,mn}(t_0+i\Delta t)+\boldsymbol{L}_s(t_0+(i-1)\Delta t)\boldsymbol{I}_s(t_0+(i-1)\Delta t)}{\boldsymbol{R}_s+\boldsymbol{L}_s(t_0+i\Delta t)} \\
\Rightarrow \boldsymbol{R}_s &= \begin{bmatrix} \boldsymbol{R}_1 & \boldsymbol{0} & \cdots & \boldsymbol{0} \\ \boldsymbol{0} & \boldsymbol{R}_2 & \cdots & \boldsymbol{0} \\ \vdots & \vdots & \ddots & \vdots \\ \boldsymbol{0} & \boldsymbol{0} & \cdots & \boldsymbol{R}_{m_{\max}} \end{bmatrix}, \boldsymbol{R}_m = \begin{bmatrix} R_{m1} & 0 & \cdots & 0 \\ 0 & R_{m2} & \cdots & 0 \\ \vdots & \vdots & \ddots & \vdots \\ 0 & 0 & \cdots & R_{mn_{\max}} \end{bmatrix} \\
\Rightarrow \boldsymbol{E}_{s,mn} &= \begin{bmatrix} E_{11} & E_{12} & \cdots & E_{m_{\max}n_{\max}} \end{bmatrix}^T \\
\Rightarrow \boldsymbol{L}_s &= \begin{bmatrix} \boldsymbol{L}_{11} & \boldsymbol{L}_{12} & \cdots & \boldsymbol{L}_{1m_{\max}} \\ \boldsymbol{L}_{21} & \boldsymbol{L}_{22} & \cdots & \boldsymbol{L}_{2m_{\max}} \\ \vdots & \vdots & \ddots & \vdots \\ \boldsymbol{L}_{m_{\max}1} & \boldsymbol{L}_{m_{\max}2} & \cdots & \boldsymbol{L}_{m_{\max}m_{\max}} \end{bmatrix}, \boldsymbol{L}_{ij} = \begin{bmatrix} L_{\mathrm{self},j1} & M_{i1,j2} & \cdots & M_{i1,jn_{\max}} \\ M_{i2,j1} & L_{\mathrm{self},j2} & \cdots & M_{i2,jn_{\max}} \\ \vdots & \vdots & \ddots & \vdots \\ M_{in_{\max},j1} & M_{in_{\max},j2} & \cdots & L_{\mathrm{self},jn_{\max}} \end{bmatrix}
\end{aligned}
\tag{A.5}
$$

where t_0 represents the initial moment, $\boldsymbol{R}_s$, $\boldsymbol{E}_s$ and $\boldsymbol{L}_s$ are the resistance, induced voltage and inductance matrices of the nested-loops, respectively. $\boldsymbol{R}_s$ can be derived from the material resistivity and physical structure. $\boldsymbol{E}_s$ and $\boldsymbol{L}_s$ can be solved by the secondary voltage and inductance models.

REFERENCES

[1] W. Xu, R. Islam, and M. Pucci, *Advanced Linear Machines and Drive Systems*, Springer-Verlag Berlin Heidelberg, Sep. 2019.

[2] W. Xu, X. Xiao, and G. Du *et al*, "Comprehensive Efficiency Optimization of Linear Induction Motors for Urban Transit," *IEEE Trans. Veh. Technol.*, vol. 69, no. 1, pp. 131–139, Nov. 2019.

[3] C. Kan, J. Zhang, and B. Ma *et al*, "Design and Simulation on a New Type Linear Brushless Doubly-fed Machine," *Micromotors*, vol. 12, no. 48, pp. 11-16, Dec. 2015.

[4] F. Saifkhani and A. K. Wallace, "A Linear Brushless Doubly-fed Machine Drive for Traction Applications," in *Proc. of Fifth European Conference on Power Electronics and Applications (EPE'93 ECCE Europe)*, Brighton, UK, Sep. 1993, pp. 344-348.

[5] F. Saifkhani, "Investigation, Analysis and Design of the Linear Brushless Doubly-fed Machine," M. S. dissertation, Dept. Electrical and Computer Engineering, Oregon State University, Oregon, USA, 1991, pp. 121-136.

[6] J. Ge, "End Effect and Characteristic Analysis for Linear Doubly fed Machine with Nested-loop Secondary," M. S. dissertation, Sch. Electrical and Electronic Engineering, Huazhong University of Science and Technology, Wuhan, CN, 2020, pp. 9-13.

[7] J. Ge, W. Xu, and Y. Liu *et al*, "Investigation on Winding Theory for Short Primary Linear Machines," *IEEE Trans. Veh. Technol.*, vol. 70, no. 8, pp. 7400-7412, Aug. 2021.

[8] J. Ge, W. Xu, and Z. Bao *et al*, "Analysis of end Effect on Thrust Ripple in Linear Brushless Doubly-fed Machine," *Proc. of International Electrical Engineering Congress (iEECON)*, Khon Kaen, TH, Mar. 2022, pp. 1-4.

[9] I. Boldea, L. N. Tutelea, and W. Xu *et al*, "Linear Electric Machines, Drives, and Maglevs: an Overview," *IEEE Trans. Ind. Electron.*, vol. 65, no. 9, pp. 7504–7515, Sep. 2018.

[10] I. Eguren, G. Almandoz, and A. Egea *et al*, "Linear Machines for Long Stroke Applications—a Review," *IEEE Access*, vol. 8, pp. 3960–3979, Dec. 2020.

[11] C. Lee and C. Chin, "A Theoretical Analysis of Linear Induction Motors," *IEEE Trans. Power App. Syst.*, vol. PAS-98, no. 2, pp. 679–688, Mar. 1979.

[12] C. Li, L. Zhao, and Q. Li *et al*, "Wavelet Transform Applied in Analyze The End-effect of Linear Motor," *Proc. of International Conference on Logistics Systems and Intelligent Management (ICLSIM)*, Harbin, CN, Jan. 2010, pp. 615-618.

[13] J. Lu and W. Ma, "Research on End Effect of Linear Induction Machine For High-speed Industrial Transportation," *IEEE Trans. Plasma Sci.*, vol. 39, no. 1, pp. 116–120, Oct. 2010.

[14] F. Alonge, M. Cirrincione, and F. D'Ippolito *et al*, "Parameter Identification of Linear Induction Motor Model in Extended Range of Operation by Means of Input-output Data," *IEEE Trans. Ind. Appl.*, vol. 50, no. 2, pp. 959–972, Mar. 2014.

[15] S. Yamamura, *Theory of Linear Induction Motors*, Wiley, New York, 1979.

[16] M. Inoue and K. Sato, "An Approach to a Suitable Stator Length for Minimizing the Detent Force of Permanent Magnet Linear Synchronous Motors," *IEEE Trans. Magn.*, vol. 36, no. 4, pp. 1890–1893, Jul. 2000.

[17] M. Wang, W. Xu, and C. Yang *et al*, "Analytical Calculation of No-load Magnetic Field in Permanent Magnet Linear Synchronous Motors Based on an Accurate Subdomain Model," *Transactions of China Electrotechnical Society*'', vol. 35, no. 5, pp. 942–953, Feb. 2020.

[18] T. C. O'Connell and P. T. Krein, "A Schwarz–christoffel-based Analytical Method for Electric Machine Field Analysis," *IEEE Trans. Energy Convers.*, vol. 24, no. 3, pp. 565-577, Sep. 2009.

[19] C. Carpenter, "The Application of the Method of Images to Machine End-winding Fields," *Proceedings of the IEE-Part A: Power Engineering*, vol. 107, no. 35, pp. 487–500, Oct. 1960.

Yaping Zhang was born in Shandong, China, in 1999. She received the B.E. degree in electrical engineering and automation from Northeast Forestry University, Harbin, China, in 2021.

She is currently working toward the M.E. degree in electrical engineering in Huazhong University of Science and Technology. Her research interests include linear machines, and brushless doubly-fed machines.

Jian Ge was born in Heilongjiang, China, in 1994. He received the B.E., M.E. and Ph.D degrees in electrical engineering from Huazhong University of Science and Technology, Wuhan, China, in 2016, 2019 and 2022, respectively.

He is currently a Postdoctoral Researcher in electrical engineering in

Huazhong University of Science and Technology. His research interests include induction machines, linear machines, and brushless doubly-fed machines.

Wei Xu (Senior Member'13) received the double B.E. and M.E. degrees from Tianjin University, Tianjin, China, in 2002 and 2005, and the Ph.D. from the Institute of Electrical Engineering, Chinese Academy of Sciences, in 2008, respectively, all in electrical engineering. His research topics mainly cover design and control of linear machines and drive systems.

From 2008 to 2012, he made Postdoctoral Fellow with University of Technology Sydney, Vice Chancellor Research Fellow with Royal Melbourne Institute of Technology, Japan Science Promotion Society Invitation Fellow with Meiji University, respectively. Since 2013, he has been one full professor with State Key Laboratory of Advanced Electromagnetic Engineering in Huazhong University of Science and Technology, China. He is Fellow of the Institute of Engineering and Technology (IET). He is the General Chair for 2021 International Symposium on Linear Drives for Industry Applications (LDIA 2021) and 2023 IEEE International Conference on Predictive Control of Electrical Drives and Power Electronics (PRECEDE 2023), both in Wuhan, China. He has been Editor or Associate Editor for over 10 internationally leading Journals, such as IEEE Transactions on Industrial Electronics, IEEE Transactions on Vehicular Technology, IEEE Transactions on Energy Conversion, IEEE Transactions on Industry Applications, and so on.

Hao Tang received the B.E. degree from the National University of Defense Technology, Changsha, China, in 2005. He has been a senior engineer in Xiangyang CRRC Motor Technology Co., Ltd.. His research interests include intelligent manufacturing of linear machines.

Yang Gao received the B.E. degree from Central South University, Changsha, China, in 2005 and the M.E. degree from Sun Yat-Sen University, Guangzhou, China, in 2014, respectively. He has joined the Guangzhou Metro Group Co., Ltd., since 2005. His research interests mainly include the vehicle engineering for urban rail transit.

Xiaoliang Chen, senior engineer, received the B.E. degree from the School of Electrical And Information Engineering, Dalian Jiaotong University in 2007. He received the master degree in engineering from the School of Electric Power, South China University of Technology in 2018. Since joining Guangzhou Metro Group Co., Ltd. in 2007, he has been engaged in the maintenance and technical development of linear metro.

Shihu Su received the master degree from the School of Electrical and Electronic Engineering, Huazhong University of Science and Technology, China, in 2017. He is now working with CRRC Zhuzhou Motor Co., Ltd., Zhuzhou, China, where he is responsible for the research and product development of linear machines and drives.

Zhen Bao received the B.E. degree in electrical engineering in 2021 from Hunan University, Changsha, China. He is currently working toward the Ph.D. degree with the State Key Laboratory of Advanced Electromagnetic Engineering, Huazhong University of Science and Technology, Wuhan, China.

His research interests include advanced control methods for Linear machines and brushless doubly-fed machines.